ISIJ International, Vol. 65 (2025), No. 10, pp. 1481–1492
https://doi.org/10.2355/isijinternational.ISIJINT-2025-110

Novel Bayesian Statistical Analysis on Acoustic Emission Data during Dwell-fatigue of Ti-6Al-4V Alloys

Haoyu HU,[1] Fabien BRIFFOD,[2] Takayuki SHIRAIWA[1]* and Manabu ENOKI[1]

1) Department of Materials Engineering, The University of Tokyo, 7-3-1 Hongo, Bunkyo-ku, Tokyo, 113-8656 Japan.
2) Research Center for Structural Materials, National Institute for Materials Science, 1-2-1 Sengen, Tsukuba, Ibaraki, 305-0047 Japan.

(*Received March 31, 2025; Accepted July 22, 2025; Advance online published July 30, 2025; Published September 15, 2025*)

Load hold at peak stress can drastically reduce the fatigue life of Ti-6Al-4V alloys, a phenomenon known as dwell-fatigue life debit. Unlike normal fatigue, dwell-fatigue exhibits a characteristic three-stage strain accumulation curve: an initial rapid strain increase (primary), followed by a steady strain-increase (secondary), and finally an accelerated stage leading to failure (tertiary). In the current study, flat specimens made out of three distinct microstructures of Ti-6Al-4V alloys were subjected to uniaxial fatigue load with 120-second peak stress hold and 0.1 load ratio with real-time acoustic emission (AE) measurement. The microstructures, namely, equiaxed, bimodal, and lamellar, were tailored through different heat treatment procedures. Bayesian statistical analysis of AE data enabled both the detection of stage transition points using Markov chain Monte Carlo (MCMC) simulation and the selection of strain accumulation models through replica MCMC method. The results demonstrated that two change-points detected showed strong correlation with the transitions in the creep-like three-stage curve of strain accumulation. The strain accumulation behavior was successfully predicted using AE parameters. Furthermore, average frequency proved crucial in monitoring the beginning of dwell-fatigue process.

KEY WORDS: Ti-6Al-4V alloys; dwell-fatigue; acoustic emission; strain accumulation; Bayesian statistics.

1. Introduction

Titanium alloys are widely used in deep-sea equipment, aerospace components, and biomedical applications due to their superior properties, including high strength, excellent fatigue and creep resistance at elevated temperatures, favorable strength-to-weight ratio, high corrosion resistance, and biocompatibility.[1,2] Among various titanium alloys, Ti-6Al-4V is particularly significant, representing more than 50% of the worldwide titanium production.[3] Components manufactured from Ti-6Al-4V alloys frequently operate under demanding thermal and mechanical conditions, including cyclic loading and load-holding at high stress levels.[1,4] A drastic reduction in fatigue life due to load hold, termed dwell-fatigue life debit, has been widely reported in Ti-6Al-4V alloys.[1,4–7] Unlike the limited strain accumulation in conventional fatigue, dwell-fatigue exhibits significant time-dependent strain accumulation.[8] This strain evolution typically follows a characteristic three-stage pattern similar to creep behavior: an initial primary stage with decreasing strain rate, followed by a steady-state secondary stage, and concluding with an accelerating tertiary stage leading to failure.[1,7,9]

Acoustic emission (AE) refers to the phenomenon of sound or ultrasound wave radiation in solids resulting from a sudden release of energy. These energy releases can originate from various sources, including plastic deformation, crack initiation and propagation, and phase transformation. The generated elastic waves are detected by piezoelectric transducers attached to the solid surface.[10–13] AE analysis typically involves characterizing individual events through signal parameters. Waveform extraction is performed using a threshold-based approach, with each extracted waveform considered an independent event.[10,12] Common AE parameters include amplitude, count, duration, rise time, energy, and various frequency characteristics.[12,14,15]

Leveraging the real-time monitoring capability of AE, researchers have attempted to monitor fatigue processes in metallic materials. Particular emphasis has been placed on predicting fatigue life through AE analysis, often establishing empirical correlations between AE parameters and crack growth behavior.[12,14,16] Roberts and Talebzadeh proposed a relationship between AE count rate and crack growth rate.[14] Yu *et al.* later argued that cumulative absolute energy

---

* Corresponding author: E-mail: shiraiwa@rme.mm.t.u-tokyo.ac.jp

rate provided more suitable predictions than count rate.[16] Shiraiwa *et al.* further advanced this approach by proposing crack growth models as the sum of power terms of multiple AE parameters, with optimal models selected through Bayesian inference. These multi-parameter models demonstrated superior accuracy compared to single-parameter approaches.[12]

Despite extensive AE research in conventional fatigue, studies on dwell-fatigue of titanium alloys utilizing AE analysis remain limited. McBagonluri *et al.*[17] demonstrated a linear relationship between counts/energy and time during dwell-fatigue of Ti-6242, suggesting crack initiation in the first cycle with crack propagation as the primary deformation mechanism throughout the remaining dwell-fatigue life. However, their study lacked AE data filtering to eliminate noises, which was considered a crucial part in dealing with AE data.[14,16,18] Another research carried out by J.E. Hack and G.R. Leverant[19] attempted to use AE for detecting cracking during dwell-fatigue, but detected only three events with minimal analytical discussion. To address this lack of comprehensive AE research on dwell-fatigue, this study aims at developing a novel Bayesian statistical framework for monitoring the substantial strain accumulation during dwell-fatigue of Ti-6Al-4V alloys. The framework includes change-point detection dividing strain accumulations into three stages and the selection of optimal multi-parameter models for predicting strain accumulation based on AE data, both of which will be achieved by Markov chain Monte Carlo (MCMC) simulations.

2. Materials and Methods

2.1. Materials and Heat Treatment

A commercial Ti-6Al-4V sheet, provided by *Tokyo Titanium Co.*, was used in this study. The chemical composition is shown in **Table 1**.

The as-received material served as one microstructure type (designated as EQ). Two additional heat treatment procedures were applied to the as-received material to achieve different microstructures, as shown in **Fig. 1**. Annealing below β-transus (900°C) followed by air cooling (AC) generated bimodal structures (designated as BM). For fully lamellar structures (designated as LM), the material was annealed at 1 010°C for 3 minutes, followed by 10 minutes of furnace cooling (FC) and subsequent air cooling. All samples (EQ, BM, and LM) underwent final tempering at 700°C for two hours.

Table 1. Chemical composition (mass%) of Ti-6Al-4V alloy used in this study.

Al	V	O	Fe	C	N	H	Ti
6.00	4.06	0.11	0.15	0.02	0.006	0.005	Bal.

Microstructural observations were conducted using a laser microscope (LEXT OLS4000, Olympus, Japan). Specimens from both heat treatment conditions and the as-received state were mechanically polished up to #4000 grit sandpaper, followed by final polishing with 0.05 μm oxide polishing solution. The polished specimens were then etched in a mixed solution of 8% HNO_3 (nitric acid) and 2% HF (hydrofluoric acid) for 10 seconds to reveal the microstructures. Moreover, electron back-scatter diffraction (EBSD) measurements were performed to further characterize the microstructural information of each condition. Specimens were prepared by final polishing with colloidal silica suspension for more than 5 hours. EBSD data were collected using a Schottky field emission SEM (JSM-7900F, JEOL, Japan) equipped with an EBSD detector (Symmetry, Oxford Instruments, UK).

2.2. Mechanical Test Methods

Fatigue tests, including pure fatigue and dwell-fatigue tests, were conducted on dog-bone shaped specimens with the geometry shown in **Fig. 2**(a). All mechanical testings were performed using an electrohydraulic servo fatigue testing machine (Servopulser 50kN, Shimadzu, Japan), with the experimental setup illustrated in Fig. 2(b). The tests were conducted with simultaneous *in-situ* surface observation and real-time AE measurement.

The *in-situ* surface observations served two purposes: macroscopic strain measurement and surface crack tracking. Surface imaging was conducted using a digital microscope (VHX-5000, KEYENCE, Japan) equipped with a long-focal-distance zoom lens (VH-Z50L, KEYENCE, Japan, 50X-500X) mounted on a 3-axial moving stage, as shown in Fig. 2(b). The X-stage movement for auto-focusing was controlled by a 3D measurement unit (VHX-S15C, KEYENCE, Japan), while Y- and Z-stage movements were regulated by a 3-axial controller (QT-ADM3, CHUO-SEIKI, Japan). A programmable controller (KV-5000, KEYENCE, Japan)

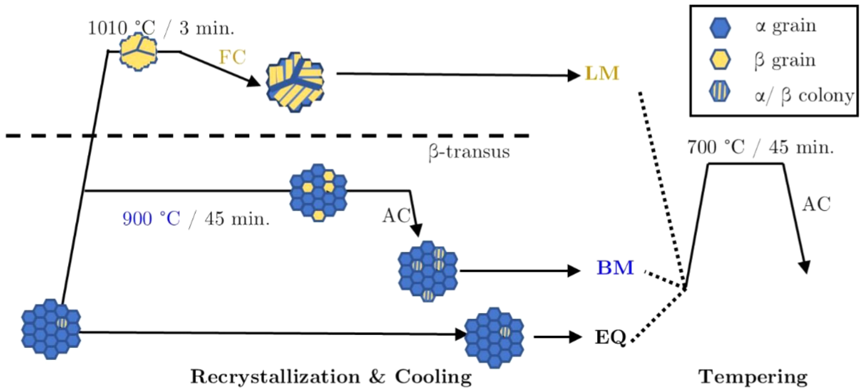

Fig. 1. Heat treatment procedures for three microstructures: equiaxed (EQ), bimodal (BM), and lamellar (LM). AC standing for air colling, FC representing furnace cooling. (Online version in color.)

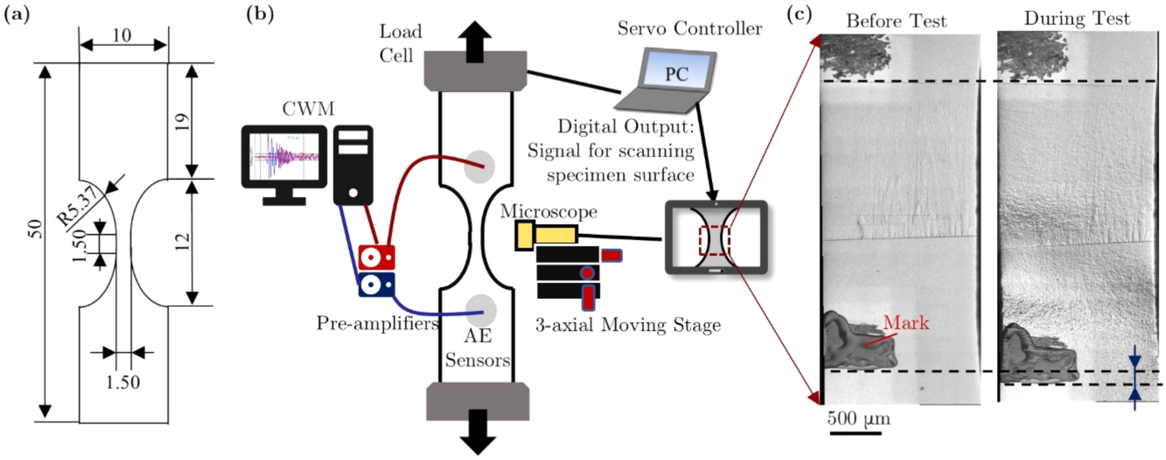

Fig. 2. (a) The geometry of the flag dog-bone specimens. (b) A schematic illustration of experimental setups. (c) An example demonstrating the macroscopic strain measurement. (Online version in color.)

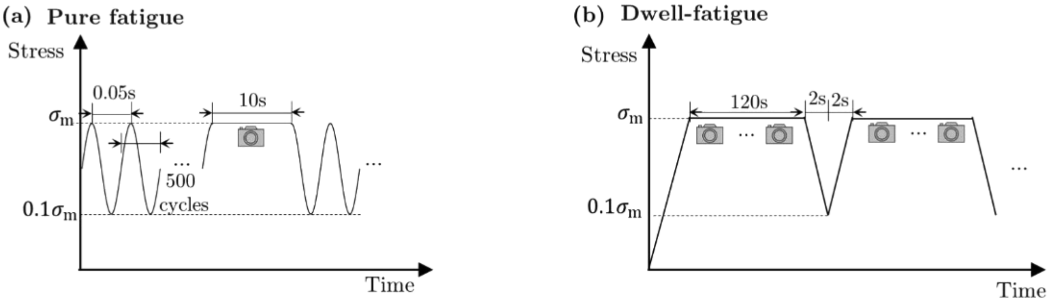

Fig. 3. Load waveforms for (a) pure fatigue and (b) dwell-fatigue tests.

coordinated the sequential operation of all components based on our customized timing protocol. Specifically, the controller received signals from the servo controller at predetermined intervals to initiate surface observations during testing.

Regarding the macroscopic strain measurement, reference marks were made at both ends of the reduced section for strain measurement. An example is shown in Fig. 2(c). The images were captured before and during testing for tracking the reference marks. In detail, strain evolution throughout testing was calculated by tracking the positions of these marks using MATLAB's Video Labeler application.

For AE measurements, two AE sensors (R-CAST M304A, FUJI Ceramics, Japan) with a resonance frequency of 300±20% kHz were attached in the vicinity of the reduced section. The detected signals were amplified through pre-amplifiers (A1002 Preamp, FUJI Ceramics, Japan) and recorded by a continuous waveform memory (CWM) system. The CWM system enabled post-filtering of the signals, eliminating the risk of data loss due to inappropriate pre-set thresholds.[20] AE measurements were conducted exclusively during dwell-fatigue testing with a sampling rate of 5 MHz.

For pure fatigue testing, sinusoidal waveform loading was applied to the specimens, as shown in **Fig. 3**(a). The load ratio and frequency were set to 0.1 and 20 Hz, respectively, for all tests. Multiple tests at different stress levels were conducted on each microstructure to establish S-N curves, with the applied peak stress conditions summarized in **Table 2**. These stress levels were determined based on the results of preliminary tensile and fatigue tests for each microstructure and were selected to cover a range of fatigue lives and to enable a comparison of dwell-fatigue behavior among the different microstructures under similar pure fatigue life conditions. Surface observations during pure fatigue testing were limited to single image captured every 500 cycles at 50X magnification to shorten the load hold at peak stress, minimizing the dwell-hold effects. AE measurements were not conducted during pure fatigue testing as the focus of AE in this study was on dwell-fatigue monitoring.

Table 2. Summary of maximum stresses for pure fatigue tests (unit: MPa).

Microstructure	Load 1	Load 2	Load 3	Load 4	Load 5	Load 6	Load 7
EQ	790	830	870	890	–	–	–
BM	790	810	820	830	860	–	–
LM	770	785	800	805	825	830	860

For dwell-fatigue testing, specimens were subjected to a trapezoidal waveform with a 120-second hold at peak stress, as shown in Fig. 3(b). The loading and unloading times were each 2 seconds, and the load ratio was maintained at 0.1. Due to the time-intensive nature of dwell-fatigue testing, a limited number of tests were conducted: two stress levels for EQ (870 and 790 MPa) and LM (805 and 785 MPa), and one stress level for BM (820 MPa). During each load holding period, a series of 14 photos (2-by-7 array) were captured at 400X magnification. These images were subsequently stitched together for macroscopic strain measurement and crack analysis. AE measurements were conducted for one test condition per microstructure: EQ at 870 MPa, BM at 820 MPa, and LM at 785 MPa.

3. Analytical Methods

3.1. Extraction and Filtering of AE Events

Two filtering processes were applied to the AE data: spatial filtering and noise filtering. For spatial filtering, a one-dimensional AE source location was assumed, and only events occurring within the reduced section (between two AE sensors) were retained. The filtering criteria were established through pencil lead breaking tests conducted outside the reduced section prior to dwell-fatigue testing. These calibration tests demonstrated that AE events from pencil lead breaks hit the sensors sequentially, with a time of arrival (TOA) difference of 3.3 ± 0.3 μs. Consequently, AE events during dwell-fatigue testing with TOA differences exceeding 3.3 μs were filtered out.

Noise filtering was implemented to eliminate machine-induced interference. Continuous background noise was removed using a 47 dB threshold. Additionally, transient noise signals, typically below 60 dB, were observed in the 10-second period before unloading. To address this, a higher threshold of 60 dB was applied specifically during this period.

3.2. MCMC Detection of Change-points

3.2.1. Poisson Process Based Model

Change-points dividing the dwell-fatigue process into distinct stages were detected using a Poisson process model, following approaches similar to previous studies.[11,12] The model parameters were determined through MCMC sampling. The analysis considered the time of arrival (TOA) of AE events $\{t_1, t_2, \ldots, t_i, t_{i+1}, \ldots, t_S\}$ and the intervals between consecutive TOAs $\{\tau_1, \tau_2, \ldots, \tau_i, \ldots, \tau_{S-1}\}$ during dwell-fatigue testing as successive time-series data, where S represents the total number of filtered events. Based on the assumption that AE events from different sources exhibit distinct activity levels (*i.e.* λ) within particular stages, the occurrence of events within each stage was modeled as a unique Poisson process. Therefore, the models with m change-points (and $m+1$ stages) can read as follows:

$$p(\tau_i) = \lambda e^{-\lambda \tau_i} \quad \text{(1)}$$

$$\lambda = \begin{cases} \lambda_1, & C_0 < t_i < C_1 \\ \lambda_2, & C_1 < t_i < C_2 \\ \lambda_{m+1}, & C_m < t_i < C_{m+1} \end{cases} \quad \text{(2)}$$

where C_0 and C_{m+1} are the beginning and end of AE recording, $C_1, C_2, \ldots, C_m$ are the change-points between them. p is the probability of waiting time. A schematic is shown in **Fig. 4**.

The posterior distribution of the model parameters was determined using Bayes' rule:

$$p(\theta_i \mid D) = \frac{p(D \mid \theta_i) p(\theta_i)}{\sum_i p(D \mid \theta_i) p(\theta_i)} \quad \text{(3)}$$

where θ_i represents the model parameters to be sampled. Previous studies[11,12] treated both the change-points $\{C_1, C_2, \ldots, C_m\}$ and the activity levels $\{\lambda_1, \lambda_2, \ldots, \lambda_{m+1}\}$ as independent parameters of the model. However, the potential correlation between these two sets of parameters remained unexplored. Given that strong correlations among sampled parameters can impact MCMC performance,[21] an investigation of parameter correlations was warranted.

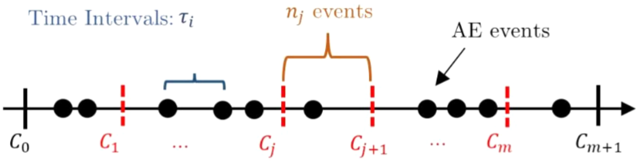

Fig. 4. Schematic of the Poisson process based change-point models. (Online version in color.)

For the likelihood function definition, consider the *j-th* stage between chang-points C_j and C_{j+1}, containing n_j AE events with i_j as the first event within this stage. The likelihood of the *j-th* stage is defined as:

$$L_j = ln \prod_{i=i_j}^{i=i_j+n_j} \lambda_j e^{-\lambda_j \tau_i} = n_j ln\lambda_j - \lambda_j \sum_{i=i_j}^{i=i_j+n_j} \tau_i \quad \text{(4)}$$

To maximize the posterior probability according to Bayes' rule, we maximize the likelihood function. The maximum value occurs when the derivative of L_j with respect to λ_j equals zero:

$$\frac{\partial L_j}{\partial \lambda_j} = \frac{n_j}{\lambda_j} - \sum_{i=i_j}^{i=i_j+n_j} \tau_i = 0 \quad \text{(5)}$$

This yields:

$$\lambda_j = \frac{n_j}{\sum_{i=i_j}^{i=i_j+n_j} \tau_i} \quad \text{(6)}$$

Since the AE time-series data is fixed, both n_j and i_j re determined by the change-points C_j and C_{j+1}. Consequently, n_j and i_j are functions of C_j and C_{j+1}, making λ_j is a function of these change-points as well.

The total likelihood of the model is therefore the sum of individual stage likelihoods:

$$L = L_1 + L_2 + \ldots + L_{m+1} = \sum_{j=1}^{j=m+1} \left(n_j ln\lambda_j - \lambda_j \sum_{i=i_j}^{i=i_j+n_j} \tau_i \right) \quad \text{(7)}$$

where λ is given by Eq. (6).

3.2.2. Sampling Algorithm

The Metropolis-Hasting (MH) algorithm was employed for MCMC sampling to detect change-points. The sampling procedure began with establishing initial parameters $\theta^0 = \left\{C_1^0, C_2^0, \ldots, C_m^0\right\}$. Since a converged Markov chain reaches the same stationary distribution regardless of initial states,[22] the initial change-points were simply distributed uniformly across the duration of dwell-fatigue testing.

The candidate parameter set $\theta^* = \left\{C_1^*, C_2^*, \ldots, C_m^*\right\}$ was generated using a proposal density based on the current state θ^k. Specifically, each new change-point candidate C_j^* was drawn from a normal distribution (q_j^k) centered at C_j^k with standard deviation σ. The sampling process for C_j^* was proposed repeatedly until was repeated until the candidate fell between adjacent change-points C_{j-1}^k and C_{j+1}^k. During the burn-in period, σ remained constant at σ_0. Subsequently,

σ was "quenched" with temperature T_q to accelerate convergence. The standard deviation σ at step k was given as:

$$\sigma = \begin{cases} \sigma_0 & , \quad k \le K_{burn-in} \\ \sigma_0 exp\left(-\dfrac{k-K_{burn-in}}{T_q}\right), & otherwise \end{cases} \quad \text{........ (8)}$$

The next step involved determining whether to accept the candidate θ^*. The acceptance ratio $\mathcal{A}$ was calculated based on the detailed balance condition:

$$\mathcal{A}\left(\theta^*,\theta^k\right) = min\left\{\frac{L\left(\theta^*\right)Q\left(\theta^k \mid \theta^*\right)}{L\left(\theta^k\right)Q\left(\theta^* \mid \theta^k\right)},1\right\} \quad \text{.......... (9)}$$

where L is the likelihood given by Eq. (7), $Q(\theta^* \mid \theta^k)$ represents the product of normal distributions (q_j^k) with C_j^k as mean values, and $Q(\theta^k \mid \theta^*)$ represents the product of normal distributions (q_j^*) with C_j^* as the mean values. The acceptance ratio $\mathcal{A}$ was compared with a random number u drawn from uniform distribution $U(0,1)$. The candidate was accepted ($\theta^{k+1}=\theta^*$) if $\mathcal{A}>u$, and rejected ($\theta^{k+1}=\theta^k$) otherwise.

The process then continued by incrementing k and returning to the second step until the desired number of iterations was achieved.

Based on previous studies showing that strain accumulation exhibits characteristic three-stage behavior during dwell-fatigue,[9,23] change-point models with two change-points were evaluated to determine stage transitions. AE events from the first and last cycles were excluded from the analysis due to intense acoustic activity associated with initial deformation and final rupture. Including these highly concentrated AE events would effectively create additional stages at the beginning and end of the test, potentially obscuring the underlying three-stage behavior of interest.

3.3. MCMC Prediction of Strain Accumulation from AE Parameters

3.3.1. Selection of AE Parameters and Proposed Model Candidates

Following the identification of distinct stages in dwell-fatigue behavior, strain accumulation rate was modeled using selected AE parameters. The first step involved identifying AE parameters with minimal correlation to ensure model robustness. Correlation coefficients were calculated among six AE parameters: count, amplitude, duration, rise time, average frequency, and peak frequency. Analysis revealed high correlation between amplitude and both count and duration; therefore, amplitude was chosen as the representative parameter. **Figure 5**(a) illustrates the correlation among AE parameters from BM dwell-fatigue testing as an example.

Four parameters (α) were selected to construct strain accumulation rate models: amplitude (*Amp.*), rise time (*Ris.*), peak frequency (*Pk.*) and average frequency (*Ave.*). These parameters were denoted by subscripts 1 to 4 in sequence. hese parameters were sequentially denoted by subscripts 1 to 4. The following 15 model candidates were considered for the strain accumulation rate ($\dfrac{d\epsilon}{dN}$):

$$log\left(\frac{d\epsilon}{dN}\right) = \sum_{i=1,2,3,4} \delta_i c_i \left(\alpha_i\right)^{m_i} \quad \text{................ (10)}$$

where δ_i are binary indicators (0 or 1) denoting the inclusion of corresponding AE parameters in each model, as shown in Fig. 5(b).

Since strain accumulation was measured per cycle while AE events occurred at irregular intervals, a cycle-based representation of AE data was necessary. For cycles containing multiple AE events, the maximum values of AE parameters were selected. Linear interpolation was applied to cycles without AE events. Moving averages were then calculated for all parameters, followed by normalization, to generate a representative AE dataset for strain prediction modeling.

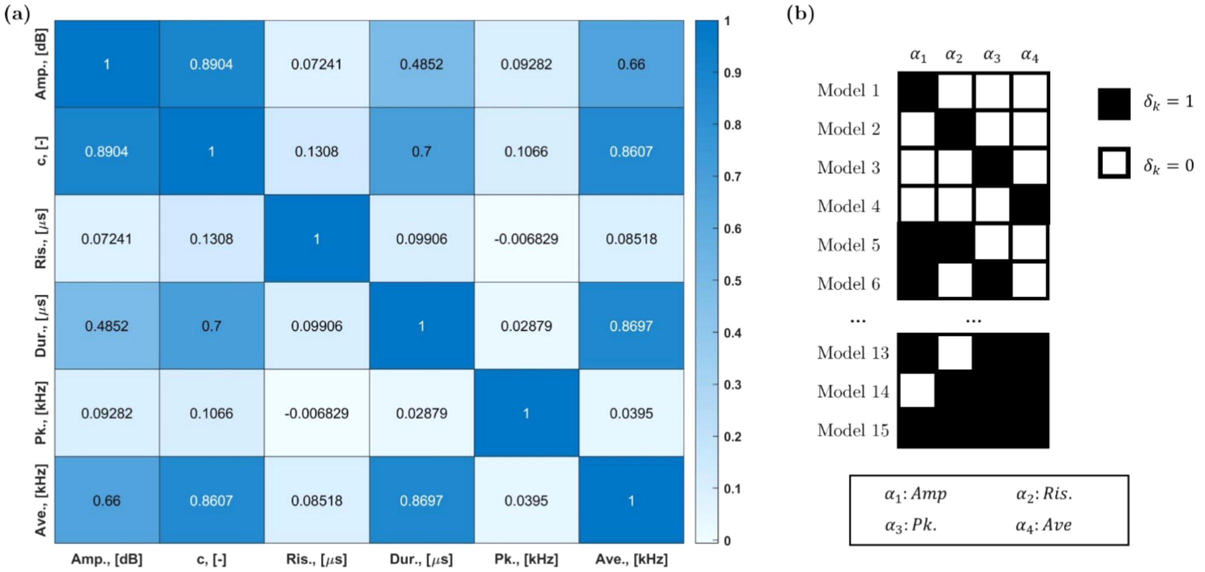

Fig. 5. (a) Heat map with correlation coefficients indicated, example taken from BM dwell-fatigue test. (b) Parameter combinations for the 15 strain accumulation rate model candidates. (Online version in color.)

3.3.2. Replica MCMC Algorithm

The MCMC simulation aims to minimize the error function $E(\theta)$:

$$E(\theta)=\frac{1}{2n}\sum_{i=1}^{n}\left(y_i-f\left(x_i;\theta\right)\right)^2 \quad (11)$$

where θ is noise variance, n is the number of data points (equal to the number of cycles), y_i is the observed value (normalized logarithmic strain rate), and $f(x_i;\theta)$ represents the prediction given by Eq. (10).

A modified approach, the replica MCMC algorithm, was employed to address local minima issues and improve model selection accuracy.[24] This method introduces an inverse temperature β ranging from 0 to 1. The posterior distribution under temperature β_l could is defined as:

$$p\left(\theta_l \mid D\right)=\frac{1}{Z(D)}exp\left(-\frac{n}{\sigma^2}\beta_l E\left(\theta_l\right)\right)\varphi\left(\theta_l\right) \quad (12)$$

where $E(\theta_l)$ is the error function under temperature β_l, $\varphi(\theta_l)$ is the prior probability and $Z(D)$ he normalization constant (evidence). The temperature β_l was defined as:

$$\beta=\begin{cases}0 & , \quad l=1\\ 1.5^{l-L_c} & , \quad otherwise\end{cases} \quad (13)$$

Low-temperature (β approaching 1) converge rapidly but are susceptible to local minima, while high-temperature chains (β approaching 0) converge slowly but better explore the parameter space. States θ_l and θ_{l+1} are exchanged following a procedure similar to the MH algorithm, with exchange ratio:

$$r=min\left\{exp\left(\frac{n}{\sigma^2}\left(\beta_{l+1}-\beta_l\right)\left(E\left(\theta_{l+1}\right)-E\left(\theta_l\right)\right)\right),1\right\} \quad (14)$$

For each Markov chain at constant temperature, the sampling process followed the MH algorithm, but with uniform distributions (centered at current values with half-lengths D_c and D_m for parameters C and m, respectively) as proposal densities.

A key advantage of replica MCMC is the straightforward calculation of stochastic complexity $F=-log(Z(D))$,[24] which serves as the model selection criterion. The model with minimum stochastic complexity is considered optimal. The stochastic complexity is computed as:

$$\begin{aligned}F &=-log\left(Z(D)\right)\\ &=\left\langle\frac{n}{\sigma^2}E(\theta)\right\rangle\\ &=\left[\left\langle\frac{n}{\sigma^2}\beta_L E\left(\theta_L\right)\right\rangle-\left\langle\frac{n}{\sigma^2}\beta_{L-1}E\left(\theta_{L-1}\right)\right\rangle\right]+\left[\left\langle\frac{n}{\sigma^2}\beta_{L-1}E\left(\theta_{L-1}\right)\right\rangle-\left\langle\frac{n}{\sigma^2}\beta_{L-2}E\left(\theta_{L-2}\right)\right\rangle\right]+\ldots\\ &\| +\left[\left\langle\frac{n}{\sigma^2}\beta_2 E\left(\theta_2\right)\right\rangle-\left\langle\frac{n}{\sigma^2}\beta_1 E\left(\theta_1\right)\right\rangle\right]\\ &=\sum_{l=1}^{L-1}\left(\beta_{l+1}-\beta_l\right)\left\langle\frac{n}{\sigma^2}E\left(\theta_l\right)\right\rangle\end{aligned} \quad (15)$$

where $\beta_L=1$, $\beta_1=0$ and $\left\langle\frac{n}{\sigma^2}E\left(\theta_l\right)\right\rangle$ is computed directly from each chain.

4. Results and Discussion

4.1. Microstructures after Heat Treatment

The microstructures of as-received and heat-treated samples are presented in **Fig. 6**. Optical microscopy revealed equiaxed microstructure in the as-received material (EQ, Fig. 6(a_1)), bimodal structure in specimens after heat treatment Pattern BM (Fig. 6(b_1)), and fully lamellar structure following heat treatment Pattern LM (Fig. 6(c_1)). These microstructural characteristics were confirmed by inverse pole figure (IPF) maps from EBSD analysis (Figs. 6(a_2)(b_2)(c_2)).

The microstructural features were quantitatively analyzed from the EBSD data. The prior β grain size was determined by reconstructing the parent grain orientation from the α phase orientation data. For the equiaxed (EQ) and bimodal (BM) microstructures, the volume fraction of primary α grains was calculated using image analysis to segment the primary α phase from the lamellar matrix, which resulted

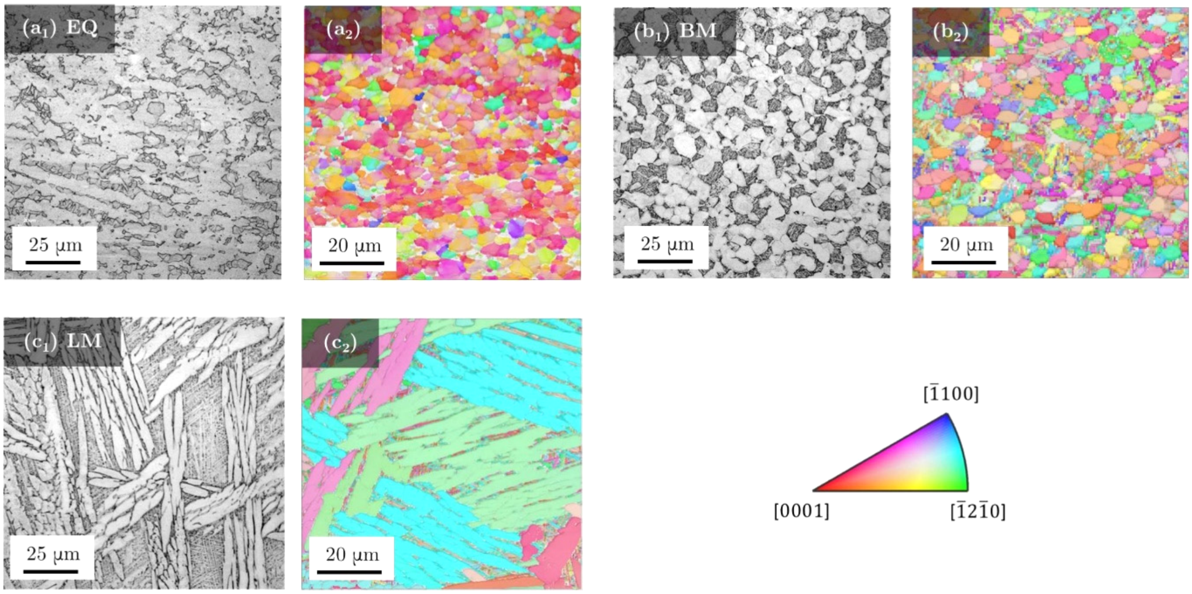

Fig. 6. Optical micrographs of (a_1) EQ, (b_1) BM, and (c_1) LM. The IPF maps of *alpha* phases of (a_2) EQ, (b_2) BM, and (c_2) LM. (Online version in color.)

in 67% for EQ and 30% for BM. The average area of prior α grains was similar in both cases, approximately 25 μm^2. Although designated as LM, the microstructure more closely resembled a bi-lamellar structure, containing both thin and thick laths measuring 1.1 μm and 6.1 μm, respectively. The average prior β grain diameter in this structure was 158.7 μm.

4.2. Pure Fatigue and Dwell-fatigue Properties

The peak stress versus cycles to failure (S-N) curves for all pure fatigue and dwell-fatigue tests are presented in **Fig. 7**(a), with empty and filled markers representing pure fatigue and dwell-fatigue data, respectively. The introduction of load holds reduced fatigue lives across all three microstructures. Comparable pure fatigue lives were observed at peak stresses of 870 MPa for EQ, 820 MPa for BM, and 805 MPa for LM, enabling direct comparison of microstructural effects on dwell-fatigue behavior. The dwell-life debit, defined as the ratio of pure fatigue life to dwell-fatigue life, was calculated at these stress levels as 1.38, 12.42, and 6 568 for EQ, BM, and LM, respectively. LM exhibited the highest dwell-life debit, followed by BM, while EQ demonstrated the highest dwell-fatigue resistance. This observation aligns with early studies that considered only lamellar microstructures as dwell-sensitive in Ti-6Al-4V alloys.[4,25)] The increasing dwell-fatigue resistance with higher volume fraction of primary α grains (0% in LM to 67% in EQ) is also consistent with previous investigations of Ti-6Al-4V alloys.[26,27)]

Strain accumulation curves for pure fatigue and dwell-fatigue tests are presented in Figs. 7(b)–7(d), with solid lines representing dwell-fatigue and dashed lines showing pure fatigue results. Higher strain accumulation was observed in dwell-fatigue compared to pure fatigue for all microstructures. Dwell-fatigue strain accumulation exhibited characteristic three-stage behavior: a primary stage with

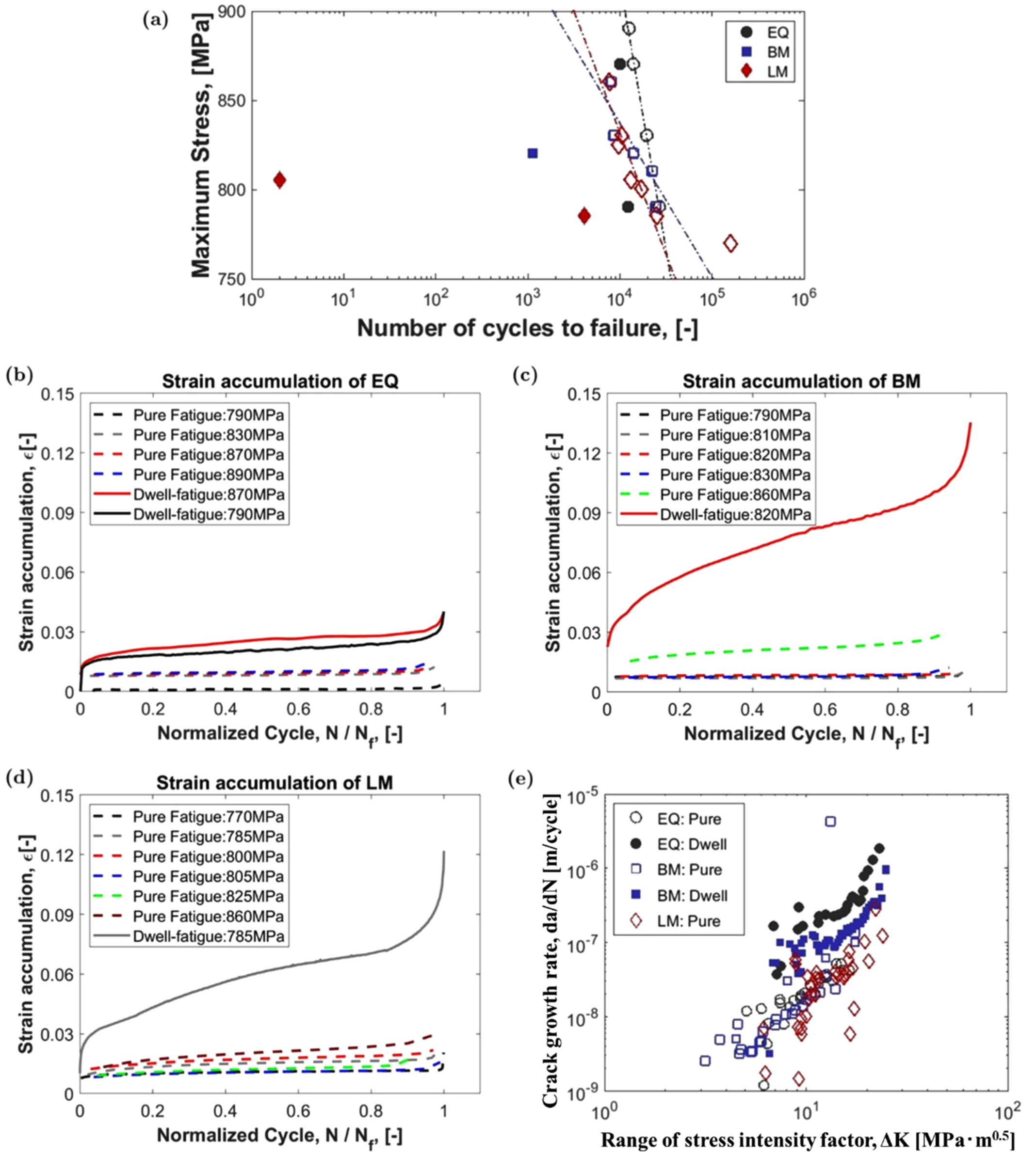

Fig. 7. (a) The S-N curves of every pure fatigue and dwell-fatigue testings performed, with filled marks denoting dwell-fatigue and empty marks denoting pure fatigue. Strain accumulation versus normalized number of cycle for (b) EQ, (c) BM, and (d) LM, with solid lines for dwell-fatigue and dash lines for pure fatigue. (e) Crack growth rate against range of stress intensity of related pure fatigue and dwell-fatigue tests. (Online version in color.)

initially high but decreasing strain rate, a secondary stage with steady strain rate, and a tertiary stage where strain rate increased until failure. In contrast, pure fatigue tests showed only a modest increase in strain rate prior to failure due to crack opening.

The *in-situ* surface observation enabled crack growth monitoring when cracks appeared on the specimen surface facing the microscope. Surface cracks were successfully observed in multiple tests: EQ specimens under both dwell-fatigue (870 MPa) and pure fatigue (790 MPa), BM specimens under both dwell-fatigue (820 MPa) and pure fatigue (810 MPa), and LM specimens under pure fatigue (770 MPa). The stress intensity factor range was calculated using the edge crack in a plate model:

$$\Delta K = \Delta\sigma\sqrt{\pi a}\left[1.12-0.23\left(\frac{a}{W}\right)+10.55\left(\frac{a}{W}\right)^{2}-21.71\left(\frac{a}{W}\right)^{3}+30.38\left(\frac{a}{W}\right)^{4}\right] \quad \text{(16)}$$

where a is the crack length, W is the plate width and $\Delta\sigma$ is the stress range.

The crack growth results are presented in Fig. 7(e). All cracks exhibited Paris law behavior in the long crack propagation region. The crack growth rates were comparable among EQ, BM, and LM microstructures under pure fatigue conditions. However, both EQ (black circles) and BM (red diamonds) showed higher crack growth rates under dwell-fatigue compared to pure fatigue conditions. Although some previous studies have reported slower long crack growth rates under dwell conditions,[17,28] our results in Fig. 7(e) showed an opposite trend. This observation, combined with the higher strain accumulation shown in Figs. 7(b)–7(d), which was suggested to introduce earlier crack initiation,[9] and faster short crack growth rate,[29] attributed to the significant life reduction under dwell-fatigue conditions. No crack growth data was obtained for the LM sample under dwell-fatigue conditions. As shown in Fig. 7(a), the fatigue life was extremely short, which made it difficult to track stable crack growth before final failure.

4.3. AE Monitoring of Dwell-fatigue Process

4.3.1. Cumulative AE Counts

After extraction and filtering, the total number of AE events recorded during dwell-fatigue tests was 834 for EQ, 1 053 for BM, and 6 795 for LM. **Figure 8** presents the cumulative AE event counts plotted against cycles, alongside strain accumulation curves. While the cumulative count curve for EQ appeared to follow the characteristic three-stage pattern, the curves for BM and LM showed significant deviation from this trend. Although AE count has been established as an effective parameter for monitoring crack growth in fatigue tests,[14,16,30,31] its sole use for monitoring strain accumulation in dwell-fatigue appears inadequate. The following sections present results from the proposed Bayesian statistical analysis framework for monitoring strain accumulation during dwell-fatigue of Ti-6Al-4V alloys.

4.3.2. Results of Change-point Detection

While strain accumulation naturally revealed three distinct stages in dwell-fatigue (Figs. 7(b)–7(d)), the primary objective of Poisson-process-based change-point detection was to identify these stages based on AE activities. The

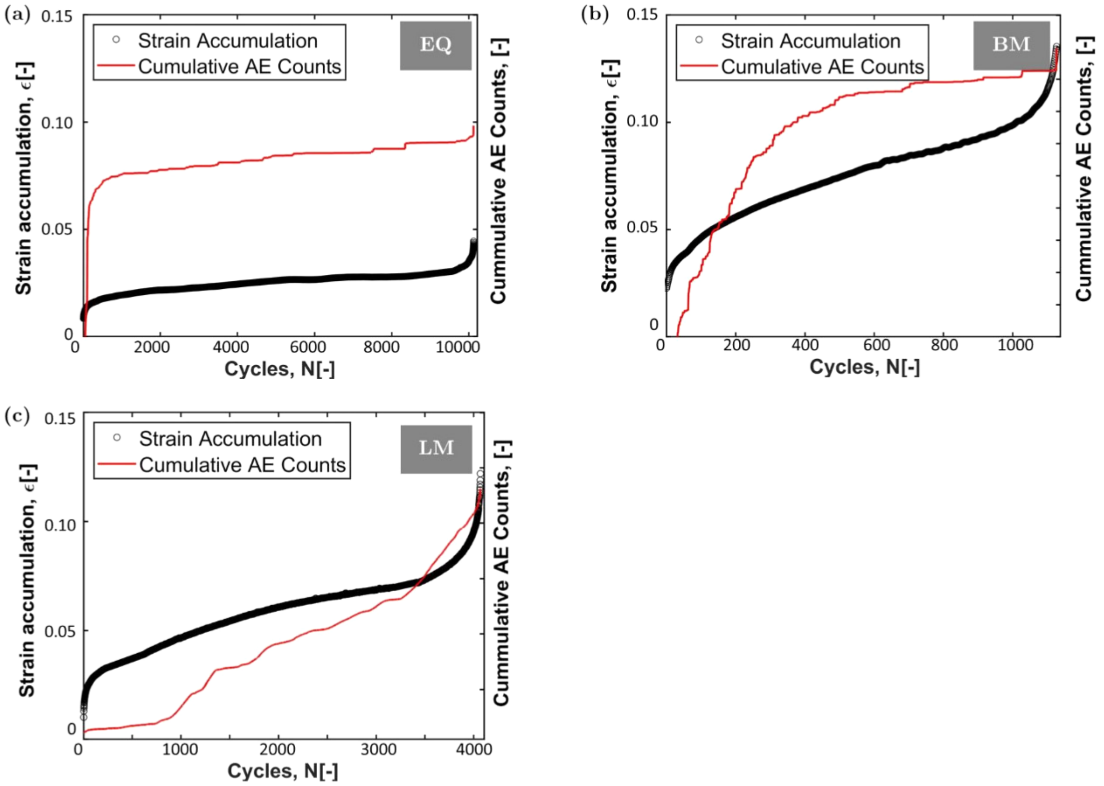

Fig. 8. Cumulative AE counts versus cycles (red lines) and strain accumulation versus cycles (black dots) for dwell-fatigue tests on (a) EQ, (b) BM, and (c) LM. (Online version in color.)

black dashed lines in **Fig. 9** presents the detected change-points by MCMC simulations, which corresponding to the modes of simulated posterior distributions (shown in dark and light blue histograms). Examining the event densities (blue starts in Fig. 9) reveals different characteristics of AE activity levels for each stage of dwell-fatigue. The primary stage is characterized by high-density AE activities, with relatively lower time difference between neighboring events. In contrast, the secondary stage exhibits notably reduced AE activities with more scattered and isolated events. As the material transitions to the tertiary stage, AE activity intensifies again with increased density prior to final failure. These characteristics were observed among three microstructures.

When overlaid with strain accumulation curves (red lines), the AE-based change-points showed strong correlation with strain accumulation transitions for all three microstructures. This correlation validates the acoustic emission approach for detecting critical stage transitions during dwell-fatigue. The posterior distributions exhibited shapes resembling normal or lognormal distributions, indicating successful convergence of the MCMC simulations. The detected change-points are summarized in **Table 3**.

4.3.3. Results of AE-parameter-based Models for Strain Accumulation Prediction

Using the detected change-points, strain prediction models based on AE parameters were selected through Bayesian inference for each stage. The stochastic complexity was calculated for all 15 model candidates listed in Eq. (10) and illustrated in Fig. 5(b), with the model exhibiting the lowest complexity being selected. The parameters of the selected models are summarized in **Table 4**.

Figures 10(a)–10(c) presents comparisons between observed strain accumulation (red lines) and predicted values derived from AE parameters (blue lines). The close agreement between predictions and observations demon-

Table 3. Summary of change-points detected in dwell-fatigue tests.

Microstructure	1st change-point	2nd change-point	Life
EQ	546	9 722	10 106
BM	50	1 049	1 127
LM	192	3 317	4 071

Table 4. Summary of selected parameters and models for strain accumulation prediction of each stage in dwell-fatigue tests.

Microstructure	Stage	Model	Parameters
EQ	Primary	15	*Amp., Ris., Pk., Ave.*
	Secondary	1	*Amp.*
	Tertiary	14	*Ris., Pk., Ave.*
BM	Primary	13	*Amp., Pk., Ave.*
	Secondary	7	*Amp., Ave.*
	Tertiary	1	*Amp.*
LM	Primary	12	*Amp., Ris., Ave.*
	Secondary	4	*Ave.*
	Tertiary	3	*Pk.*

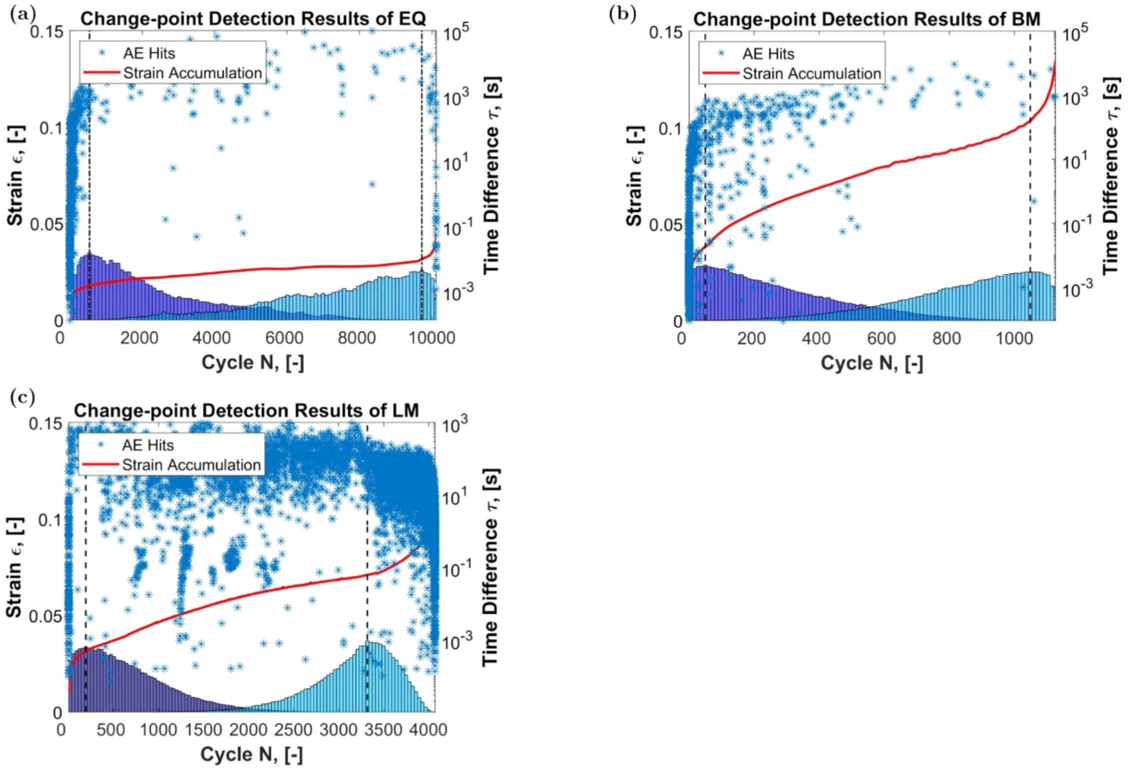

Fig. 9. Change-point detection results from MCMC simulations of AE data for (a) EQ, (b) BM, and (c) LM microstructures. Vertical dashed lines for detected change-points with corresponding posterior distributions as blue histograms. Blue stars for individual AE hits with right y-axis scale for time differences between hits. Solid red lines for strain accumulation curves with reference to left y-axis. (Online version in color.)

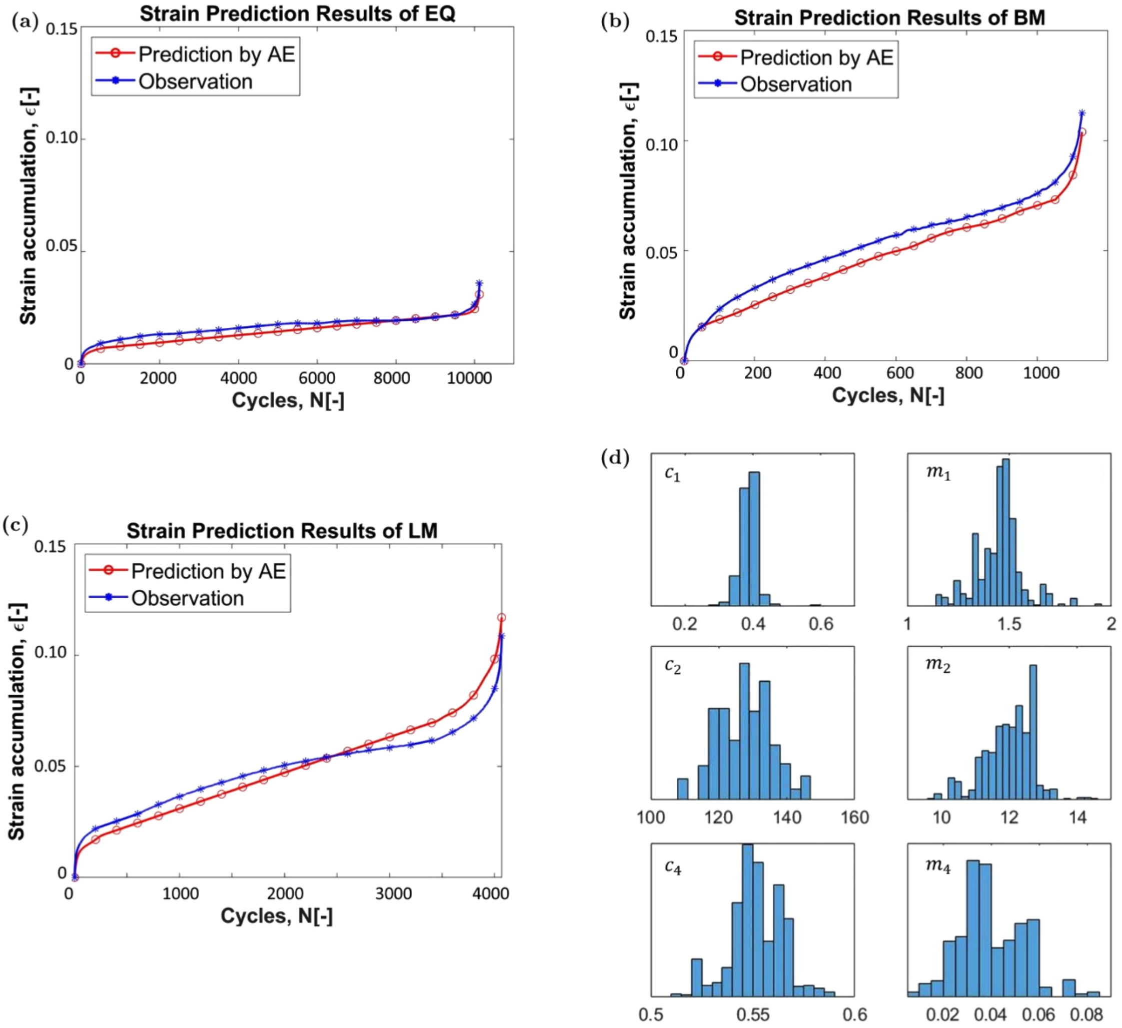

Fig. 10. Comparisons between observed (red) and predicted (blue) strain accumulations for (a) EQ, (b) BM and (c) LM. (d) Histograms showing the posterior distributions of the parameter C_i and m_i, taking the primary stage of LM as an example. (Online version in color.)

strates that strain can be effectively predicted using AE data through the proposed MCMC methods. While AE counts have been traditionally used for monitoring crack growth in conventional fatigue tests, their direct application to dwell-fatigue strain monitoring showed limitations, as demonstrated in Fig. 8. The strain prediction results in Fig. 10 demonstrate how our multi-parameter approach offers a novel solution specifically tailored to dwell-fatigue behavior. By incorporating and selecting optimal combinations of AE parameters (amplitude, rise time, peak frequency, and average frequency) through Bayesian inference, the models accurately track strain evolution through all three stages of dwell-fatigue across different microstructures.

The posterior distributions of the simulated parameters closely resembled normal distributions, demonstrating the successful convergence of MCMC simulations. Figure 10(d) provides an example from the primary stage of LM, where this characteristic distribution is clearly evident.

From Table 4, amplitude and average frequency appear in the models for the primary stage across all three microstructures. **Fig. 11** illustrates the normalized contributions of each AE parameter to strain rate prediction during the early primary stage. Certain terms function as relatively constant baselines, while others decrease with increasing cycle count. For EQ and LM (Figs. 11(a), 11(c)), the amplitude term provides this baseline, while for BM (Fig. 11(b)), peak frequency serves this function. Notably, the characteristic strain rate decrease in the primary stage correlates with the average frequency term in all three microstructures. This consistency highlights average frequency's sensitivity to the underlying physical processes governing primary stage strain evolution. It should be noted, however, that different AE parameters were selected for secondary and tertiary stages, indicating a limitation of this research in that a universal set of parameters applicable across all stages has not been identified.

4.3.4. Dwell-fatigue Mechanisms from AE Analysis

The results demonstrated that the LM microstructure exhibits the highest dwell-fatigue debit. This significant life reduction is attributed to the degradation of both crack initiation and propagation behavior under dwell loading. Our proposed AE analysis provides further insight into these mechanisms. Our previous work on a forged Ti-6Al-4V alloy revealed that dwell loading facilitates early and multiple crack initiations, originating from significant strain localization at microstructural features like colony boundaries. This mechanism is particularly relevant to the

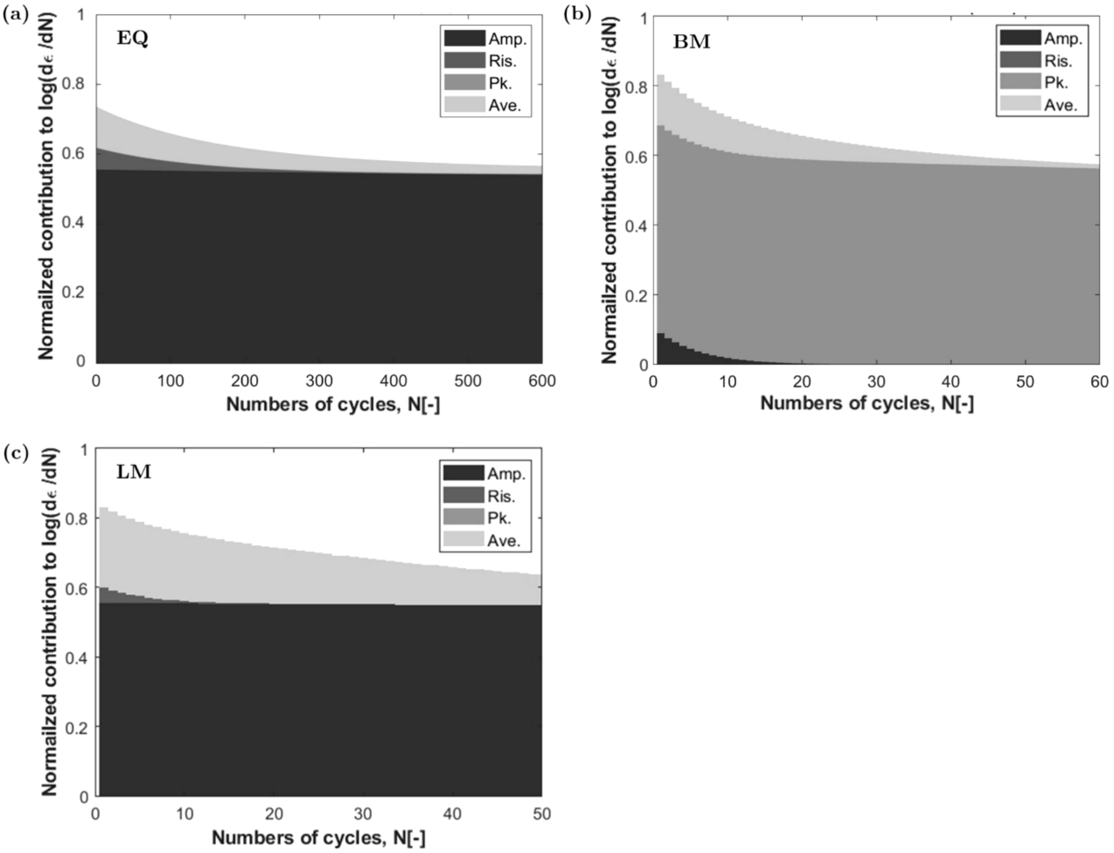

Fig. 11. Normalized contributions of AE parameter terms to strain rate prediction during early primary stage for (a) EQ, (b) BM and (c) LM microstructures.

LM microstructure, where long, straight slip paths can promote intense strain localization. Additionally, the current study shows that dwell loading also accelerates the crack propagation rate (Fig. 7(e)). The AE analysis framework captures this accelerated damage process effectively. For the LM sample, the change-point detection (Fig. 9(c)) reveals a very early transition from the primary stage (Stage I) to the secondary stage (Stage II) at only 192 cycles. Stage I, characterized by intense AE activity, corresponds to the initial rapid plastic deformation and damage accumulation leading to crack initiation. The remarkably short duration of Stage I for the LM sample strongly suggests that the process leading to crack initiation is significantly accelerated, which is the dominant factor for the massive life debit. The subsequent AE activities in Stages II and III then reflect the process of crack propagation until final failure. Therefore, while our AE-based method does not strictly separate crack initiation from propagation, it enables a semi-quantitative assessment of the damage progression. By identifying the accelerated transition between damage stages, the analysis supports the conclusion that the drastic reduction in dwell-fatigue life for the LM microstructure is primarily governed by the acceleration of the initial damage and crack initiation stage.

5. Conclusions

The present study investigated the dwell-fatigue behavior of Ti-6Al-4V alloy with three different microstructures (equiaxed, bimodal, and lamellar) by developing a novel Bayesian statistical framework for monitoring strain accumulation. This approach integrated mechanical testing, *in-situ* observation, and acoustic emission (AE) monitoring to characterize the dwell-fatigue process. The key findings of this work can be summarized as follows:

(1) When compared at similar pure fatigue life conditions, microstructure strongly influenced dwell-fatigue sensitivity, with dwell-life debits of 1.38, 12.42, and 6 568 for equiaxed, bimodal, and lamellar microstructures, respectively. The equiaxed microstructure with the highest volume fraction of primary α grains (67%) demonstrated superior dwell-fatigue resistance.

(2) Change-points corresponding to stage transitions were successfully detected using Poisson process-based MCMC simulations of AE data. These AE-derived change-points showed strong correlation with the visually observed transitions in strain accumulation.

(3) Bayesian model selection identified optimal combinations of AE parameters for strain prediction, with average frequency emerging as a consistently significant parameter in the primary stage across all microstructures. The resulting stage-specific models accurately captured strain evolution throughout the entire dwell-fatigue process, demonstrating the effectiveness of the multi-parameter approach for non-destructive monitoring of dwell-fatigue damage progression.

Statement for Conflict of Interest

The authors declare that they have no known competing financial interests or personal relationships that could have appeared to influence the work reported in this paper.

Acknowledgments

This work was supported by Council for Science, Technology and Innovation (CSTI), Cross-ministerial Strategic Innovation Promotion Program (SIP), "Materials Integration" for Revolutionary Design System of Structural Materials (Funding agency: JST), by the JSPS KAKENHI for Challenging Research Pioneering (Grant Number 23K17336), by the JSPS KAKENHI for Early-Career Scientists (Grant No. 22K14139), by the JSPS KAKENHI for Scientific Research (B) (Grant Number 21H01648), by the JSPS KAKENHI for Grant-in-Aid for Transformative Research Areas (A) (Grant Number 23H04464, 24H00982), and by ISIJ Research Promotion Grant (FY2022).

Nomenclature

a: Crack length
c_i: Coefficient in strain accumulation model
C_i: Change-point between stages
D: Dataset
D_c, D_m: Half-lengths of uniform distribution for MCMC sampling
E: Error function
F: Stochastic complexity
$f(x_i;\theta)$: Prediction function with parameters θ
k: Iteration step in MCMC simulation
$K_{burn\text{-}in}$: Burn-in period in MCMC simulation
ΔK: Range of stress intensity factor
l: Number of chain
L_c: Total number of chains in replica MCMC
L_j: Likelihood of j-th stage
L: Likelihood function
m_i: Power term exponent in strain accumulation model
n: Number of data points
N: Number of cycles
p: Probability
$p(D|\theta_i)$: Likelihood: probability of observing the data given parameters
$p(\theta_i)$, $\varphi(\theta_l)$: Prior: initial probability distribution of parameters
$p(\theta_i|D)$: Posterior: updated probability distribution of parameters given observed data
S: Total number of AE events
t_i: Time of arrival of i-th AE event
T_q: Quenching temperature for MCMC simulation
Q: Proposal density
W: Specimen width
x_i: Input variable (AE parameters)
y_i: Observed value (normalized logarithmic strain rate)
$Z(D)$: Evidence (normalization constant)
u: Random number from uniform distribution for acceptance criterion
α_i: AE parameter (amplitude, rise time, peak frequency, average frequency)
β: Inverse temperature in replica MCMC
δ_i: Binary indicator for model selection
λ: Activity level of AE events
σ: Standard deviation for proposal distribution
σ_0: Initial standard deviation
σ_m: Peak stress levels in fatigue waveloads
$\Delta\sigma$: Stress range
ϵ: Strain
τ_i: Time interval between consecutive AE events
θ: Set of model parameters
$\mathcal{A}$: Acceptance ratio

REFERENCES

1) C. Sun, Y. Li, K. Xu and B. Xu: *J. Mater. Sci. Technol.*, **77** (2021), 223. https://doi.org/10.1016/j.jmst.2020.10.063
2) D. Banerjee and J.C. Williams: *Acta Mater.*, **61** (2013), 844. https://doi.org/10.1016/j.actamat.2012.10.043
3) G. Lütjering and J.C. Williams: Titanium, Springer, (2007), 86.
4) M.R. Bache: *Int. J. Fatigue*, **25** (2003), 1079. https://doi.org/10.1016/S0142-1123(03)00145-2
5) P.O. Tympel, T.C. Lindley, E.A. Saunders, M. Dixon and D. Dye: *Acta Mater.*, **103** (2016), 77. https://doi.org/10.1016/j.actamat.2015.09.014
6) K. Mori, S. Hashimoto and M. Miyahara: *ISIJ Int.*, **61** (2021), 2666. https://doi.org/10.2355/isijinternational.ISIJINT-2021-245
7) S. Hashimoto, H. Takebe, K. Mori and M. Miyahara: *ISIJ Int.*, **63** (2023), 1774. https://doi.org/10.2355/isijinternational.ISIJINT-2023-205
8) C. Lavogiez, S. Hémery and P. Villechaise: *Scr. Mater.*, **183** (2020), 117. https://doi.org/10.1016/j.scriptamat.2020.03.031
9) H. Hu, F. Briffod, W. Yin, T. Shiraiwa and M. Enoki: *Int. J. Fatigue*, **182** (2024), 108203. https://doi.org/10.1016/j.ijfatigue.2024.108203
10) C.B. Scruby: *J. Phys. E: Sci. Instrum.*, **20** (1987), 946. https://doi.org/10.1088/0022-3735/20/8/001
11) E. Agletdinov, E. Pomponi, D. Merson and A. Vinogradov: *Ultrasonics*, **72** (2016), 89. https://doi.org/10.1016/j.ultras.2016.07.014
12) T. Shiraiwa, H. Takahashi and M. Enoki: *Mater. Sci. Eng. A*, **778** (2020), 139087. https://doi.org/10.1016/j.msea.2020.139087
13) T. Shiraiwa, K. Ishikawa, M. Enoki, I. Shinozaki and S. Kanazawa: *J. Eur. Ceram. Soc.*, **40** (2020), 2791. https://doi.org/10.1016/j.jeurceramsoc.2020.03.035
14) T.M. Roberts and M. Talebzadeh: *J. Constr. Steel Res.*, **59** (2003), 695. https://doi.org/10.1016/S0143-974X(02)00064-0
15) T. Shiraiwa, K. Tamura and M. Enoki: *Mater. Sci. Eng. A*, **768** (2019), 138473. https://doi.org/10.1016/j.msea.2019.138473
16) J. Yu, P. Ziehl, B. Zrate and J. Caicedo: *J. Constr. Steel Res.*, **67** (2011), 1254. https://doi.org/10.1016/j.jcsr.2011.03.005
17) F. McBagonluri, E. Akpan, C. Mercer, W. Shen and W.O. Soboyejo: *Mater. Sci. Eng. A*, **405** (2005), 111. https://doi.org/10.1016/j.msea.2005.05.097
18) A.Y. Iziumova, A.N. Vshivkov, A.E. Prokhorov, I.A. Panteleev, V.A. Mubassarova, O.A. Plekhov, M.L. Linderov, D.L. Merson and A. Vinogradov: *Acta Mech.*, **232** (2021), 1853. https://doi.org/10.1007/s00707-020-02911-4
19) J.E. Hack and G.R. Leverant: *Metall. Trans. A*, **13** (1982), 1729. https://doi.org/10.1007/BF02647828
20) K. Ito and M. Enoki: *Mater. Trans.*, **48** (2007), 1221. https://doi.org/10.2320/matertrans.I-MRA2007850
21) S.M. Harrington, V. Wishingrad and R.C. Thomson: *Mol. Biol. Evol.*, **38** (2021), 1627. https://doi.org/10.1093/molbev/msaa295
22) S.D. Hill and J.C. Spall: *IEEE Control Syst.*, **39** (2019), 56. https://doi.org/10.1109/MCS.2018.2876959
23) C. Lavogiez, S. Hémery and P. Villechaise: *Int. J. Fatigue*, **131** (2020), 105341. https://doi.org/10.1016/j.ijfatigue.2019.105341
24) K. Nagata, S. Sugita and M. Okada: *Neural Netw.*, **28** (2012), 82. https://doi.org/10.1016/j.neunet.2011.12.001
25) B. Wilshire and R.W. Evans: Proc. 3rd Int. Conf. Creep Fract. Eng. Mater. Struct., Institute of Materials, (1987), 603.
26) L.R. Zeng, L.M. Lei, X.M. Luo and G.P. Zhang: *J. Mater. Sci. Technol.*, **108** (2022), 244. https://doi.org/10.1016/j.jmst.2021.08.041
27) A. Ranjan, A. Singh, J.S. Jha and S.K. Mishra: *Int. J. Fatigue*, **175** (2023), 107745. https://doi.org/10.1016/j.ijfatigue.2023.107745
28) W. Shen, W.O. Soboyejo and A.B.O. Soboyejo: *Mech. Mater.*, **36** (2004), 117. https://doi.org/10.1016/S0167-6636(03)00035-8
29) S. Hémery and J.C. Stinville: *Int. J. Fatigue*, **156** (2022), 106699. https://doi.org/10.1016/j.ijfatigue.2021.106699
30) M. Chai, X. Hou, Z. Zhang and Q. Duan: *Int. J. Fatigue*, **160** (2022), 106860. https://doi.org/10.1016/j.ijfatigue.2022.106860
31) L. Li, Z. Zhang and G. Shen: *J. Mater. Eng. Perform.*, **24** (2015), 2720. https://doi.org/10.1007/s11665-015-1545-7